Toward a better understanding of peroxymonosulfate and peroxydisulfate activation using a nano zero-valent iron catalyst supported on graphitized carbon: Mechanisms and application to the degradation of estrogenic compounds in different water matrix

Minjuan Cai, Peng Cheng, Jinjun Li, Feng Wu, Mohamed Sarakha, Gilles Mailhot, Marcello Brigante

To cite this version:

Minjuan Cai, Peng Cheng, Jinjun Li, Feng Wu, Mohamed Sarakha, et al.. Toward a better understanding of peroxymonosulfate and peroxydisulfate activation using a nano zero-valent iron catalyst supported on graphitized carbon: Mechanisms and application to the degradation of estrogenic compounds in different water matrix. Journal of Cleaner Production, 2023, 414, pp.137702. 10.1016/j.jclepro.2023.137702 . hal-04129222

HAL Id: hal-04129222

https://hal.science/hal-04129222v1

Submitted on 15 Jun 2023

Toward a better understanding of peroxymonosulfate and peroxydisulfate activation using a nano zero-valent iron catalyst supported on graphitized carbon: Mechanisms and application to the degradation of estrogenic compounds in different water matrix

Minjuan Cai[a,b], Peng Cheng[b], Jinjun Li[a*], Feng Wu[a], Mohamed Sarakha[b], Gilles Mailhot[b], Marcello Brigante[b*]

[a] Department of Environmental Engineering, School of Resources and Environmental Science, Wuhan University, 430079, P. R. China

[b] Université Clermont Auvergne, CNRS, Institut de Chimie de Clermont-Ferrand, F-63000 Clermont-Ferrand, France.

Abstract

In this study, we employed nano zero-valent iron catalysts supported on graphitized carbon (GC-nZVI) catalyst to efficiently degrade BPA under circumneutral pH conditions in both dark and UVA radiation. The GC-nZVI catalyst was characterized using specific techniques (XPS, FTIR, BET, etc.), and was used to activate both PS and PMS in solution. Although no significant BPA degradation constant (k_{BPA}) was determined using PS/PMS or GC-nZVI alone, a significant synergistic effect was observed in the system. Under dark conditions, k_{BPA} increased from 0.01 min^{-1} to 0.17 when PS was used, both in the dark and under UVA. Notably, when PMS was present in the system, the improvement was even higher with k_{BPA} reaching 0.18 and 0.26 min^{-1} under dark and UVA conditions, respectively. To further support the synergistic effect, it was found that 80 % of mineralization was achieved within 2 hours of UVA exposure.

Chemical quenching experiments were conducted using selective probes and kinetic modelling showed that the activation of PS/PMS produced sulfate radicals ($SO_4^{\bullet-}$), hydroxyl radicals ($^{\bullet}OH$) and ferryl ions ($Fe^{IV}O^{2+}$) in both systems. Additionally, GC-nZVI/PMS system demonstrated good stability in recycling experiments, with up to 70 % of BPA still being degraded after 3 cycled in 1 hour under UVA.

In conclusion, the degradation efficiencies of GC-nZVI/PMS and GC-nZVI/PS systems under dark and UVA radiation were assessed for three different EDCs (BPA, E2, and EE2) in both tap and sewage treatment plant waters.

This study has demonstrated that the highly efficient GC-nZVI /PS/UVA or GC-nZVI/PMS/UVA system has significant potential for application in different water matrix, and our findings provide insights into the design of heterogeneous Fenton-like and photo-Fenton-like catalysts.

Keywords

Advanced oxidation processes, Endocrine Disrupting Compounds, Fenton-like activation, Ferryl ions, Radical formation

Introduction

Endocrine Disrupting Compounds (EDCs) are emerging environmental pollutants that include various types of natural and synthetic compounds exhibiting adverse effects on reproduction through mimicking or inhibiting the endocrine systems of animals and humans (Marty et al., 2011; Wang et al., 2020). The presence of EDCs and the resulting adverse effects in aqueous media have been widely demonstrated (Annamalai andNamasivayam, 2015; Giulivo et al., 2016; Kim et al., 2018) and various technologies to decrease their concentration including adsorption/biosorption (Ahmed et al., 2017), biochemical oxidation (Wang et al., 2022), ozonation (Esplugas et al., 2007), and treatment with hypochlorite (Romanucci et al., 2020; Zarrelli et al., 2012) have been investigated. For example, the oxidative degradation of some EDCs is associated with the aromaticity of their structures, implying that hydrophobicity may be an important feature in their study and control (Chang et al., 2009). Techniques such as treatment with activated carbon (AC) (Ghazal et al., 2022) or membranes (Kimura et al., 2004; Wijekoon et al., 2014) can effectively remove EDCs from water. However, all of these methods have some disadvantages such as long reaction times, high cost, low efficiency, incomplete removal, and production of additional toxic by-products. Recently, advanced oxidation processes (AOPs) (Jia et al., 2021a; Liu et al., 2022; Phan et al., 2022; Thomas et al., 2021) have been explored, which show great promise for the elimination of estrogenic compounds from aqueous solution, and they have been widely applied due to the non-selectivity and high redox potential of $^{\bullet}OH$.

In AOPs systems, the formation of strong and non-selective radicals such as $^{\bullet}OH$ or $SO_4^{\bullet-}$ is most prevalent. Through dehydrogenation and electron-transfer reactions between free radicals and organic pollutants, the latter are oxidized and decomposed into small molecules, ultimately being mineralized as carbon dioxide, water, and inorganic ions. $SO_4^{\bullet-}$ has similar or even higher redox potential (2.5–3.1 V) and longer half-life (30–40 μs) than $^{\bullet}OH$ (1.8–2.7 V and 20 ns respectively) (Lin et al., 2020). Moreover, its oxidation reactions can proceed efficiently over a wider pH range (from 2 to 8). Sulfate-based advanced oxidation processes (SR-AOPs) have shown excellent performances in the removal of refractory organic pollutants from aqueous environments (Giannakis et al., 2021; Jiang et al., 2019). Peroxymonosulfate (PMS) and peroxydisulfate (PS) are important sources of sulfate radicals. Due to their cost-effectiveness, good solubility, and environmentally benign, they have been widely studied and applied in environmental remediation.

Traditional activation catalysts for SR-AOPs are mainly based on transition metal ions (Jia et al., 2021b; Wu et al., 2019; Zhou et al., 2014) (Fe, Co, Mn, etc.) , or heterogeneous photoactivation (Gowrisankaran et al., 2022; Kakavandi et al., 2022; Khan et al., 2017) or ultrasound (Gujar et al., 2023). Compared to other activation methods, transition metal activation has advantages of strong activity and low energy consumption. However, single use of some of the activation techniques mentioned above can leave SR-AOPs with limitations, such as the large number of free radicals generated in a short period of time not being able to react sufficiently with the pollutant, but being quenched directly, resulting in high chemical compounds consumption, high treatment cost and low degradation efficiency of the AOPs system. The application of heterogeneous catalytic materials can enhance the generation of free radicals and promote degradation efficiency. For example, Takdastan et al. (Takdastan et al., 2018) prepared magnetite nanoparticles supported on carbon as a heterostructure catalyst and combined it with UV light and ultrasonication to efficiently activate PMS for the degradation of bisphenol A (BPA), achieving a removal efficiency of more than 90% within 30 min. Compared to energy-based activation methods, activation of PMS/PS using heterogeneous catalysts is simpler and more economical in terms of reactor/system configuration. Iron-based materials are generally regarded as excellent heterogeneous catalysts because of their non-toxicity, environmental benignity, low cost, and high catalytic activity, and so have become the most studied materials in SR-AOPs (Li et al., 2020; Xu et al., 2018; Yan et al., 2019a).

Nano zero-valent iron (nZVI), which has been widely assessed as a replacement for iron cations or iron oxides with a view to long-term use and potential reusability, has poor stability due to its high surface energy (Sun et al., 2012). To circumvent this disadvantage, stable, porous supports are usually used. The presence of carrier material also reduces the rate of oxidation of nZVI by dissolved oxygen prior to application. Carbonaceous materials have been widely used due to their high specific surface areas, adjustable pore sizes and low cost. Compared to AC, GC has abundant π-electrons and its high affinity for organics favours the adsorption of organic matter on its surface (Chen et al., 2021; Pan et al., 2021). Zhao et al. in a recent review reported that generation of $SO_4^{\bullet-}$ and $^{\bullet}OH$ can occur from the π-electrons in hybridized carbon of biochar-based catalysts to PMS (Zhao et al., 2021).

This increases the contact between them and thereby improves the degradation efficiency of AOPs. Moreover, nZVI can be uniformly dispersed on the carbon-based materials, and providing more active sites. Carbon material can also be used as a substrate for the reduction of iron oxides to nZVI. For example, Jiang et al. (Jiang et al., 2019) prepared an Fe functionalized biochar composites that consisted of ZVI, porous carbon bearing abundant functional groups, and nanofibers, which could activate PMS to efficiently remove BPA. B. Wang and co-workers (Wang et al., 2021) investigated the p-nitrophenol degradation using PS activation by n-ZVI-loaded biochar. The authors found a complete degradation after using 0.8g/L of catalysts and 1 mM of PS. Tan and al. investigated the removal of levofloxacin using nZVI/carbon fiber by achieving a good removal efficiency (~ 93 %) after 1h of reaction in the presence of 1 mM of PMS in the dark. Furthermore, they indicated that this reaction was also due to the 50% adsorption obtained during the first minutes of the reaction (Tan et al., 2021).

EDCs are represented by 17α-estradiol (EE2), 17β-estradiol (E2), and BPA. BPA is a compound showing estrogenic activity at very low concentrations, and is of prime concern with regard to water quality (Chang et al., 2009). These pollutants are stable in the environment, so it is important to evaluate their degradation in aquatic systems. In this context, the main purpose of this study is to assess the performance of nZVI supported on GC (GC-nZVI) for heterogeneous SR-AOPs at circumneutral pH values. First, the BPA degradation kinetics and steady-state concentration of different oxidant species, such as $SO_4^{\bullet-}$, $^{\bullet}OH$, and $Fe^{IV}O^{2+}$ were determined to assess their contributions to BPA degradation under thermal (dark) and UVA activation. Thereafter, the use of GC-nZVI in the presence of PS and PMS was evaluated for the degradation of E2, EE2, and BPA in tap and sewage treatment plan (STP) water samples. In our work, we use the thermal reduction of zero-valent iron with carbon and metal-catalyzed graphitization to improve the graphitization of the carbon carrier, and all the degradation data were measured after desorption. Another originality is to have differentiated the adsorption from the degradation of selected pollutants (which is not always done in other works) and to have quantified the reactive species involved in the degradation in the dark and under UVA radiation. In addition, we have shown a significant formation of the ferryl ion and determined its contribution to the selective degradation of bisphenol A in solution.

2. Materials and methods

2.1 Chemicals and irradiation setup

The list of chemicals and photochemical setup are provided in Supplementary Material

2.2 Synthesis and characterization

Ferric nitrate nonahydrate ($Fe(NO_3)_3{\cdot}9H_2O$; 6.06 g, 9.09 or 12.12 g) was first dissolved in Milli-Q water (25 mL) and then 3.0 g commercial activated carbon (from Sinopharm Chemical Reagent Co., Ltd.; 3.0 g, giving Fe:C ratios $[Fe]/[C]_n$ of 0.06:1, 0.09:1, and 0.12:1, respectively) was added. Each mixture was stirred at room temperature for 60 min, and then heated and stirred at 60 °C to evaporate the water, leaving a black solid. Each solid was placed in a corundum reactor in a tubular furnace and heated for 1 h at 250 °C under a nitrogen flow of 30 mL min^{-1}, then heated to 900 °C at a rate of 10 °C min^{-1} and maintained at this temperature for 2 h. Thereafter, it was allowed to cool naturally to room temperature. To determine the total iron in the obtained samples, portions (5 mg) were dissolved in concentrated HCl (30 mL). Each experiment was performed in duplicate. Chemical analysis was performed with an Inductively Coupled Plasma Optical Emission Spectroscopy (ICP-OES) analyzer (5800 Agilent) in radial and axial modes, using a wavelength of 238.2 nm for the quantitative determination.

The actual Fe:C ratios ($[Fe]/[C]_n$ = 0.06, 0.09 and 0.12) in the samples was measured as 0.054, 0.073, and 0.096, respectively. So, the samples are denoted as 0.05-GC-nZVI, 0.07-GC-nZVI, and 0.10-GC-nZVI, respectively.

Functional groups on the surfaces of the samples were characterized by Fourier transform infrared spectroscopy (FTIR, PerkinElmer 1725X, USA). The valence states of the constituent elements were determined by X-ray diffraction (XRD) analysis, (D8 Advance, Bruker, Germany) and X-ray photoelectron spectroscopy (XPS, Thermo-Fisher ESCALAB Xi+, USA), and binding energies were calibrated with reference to the C 1s peak at 284.8 eV. Specific surface areas were analyzed by recording Brunauer–Emmett–Teller (BET) nitrogen–adsorption-desorption isotherms. The morphological and textural properties of the samples were characterized by field–emission scanning electron microscopy (SEM; Tescan Mira3, Czech Republic, equipped with a Zeiss Sigma 300 analyzer) and transmission electron microscopy (TEM; H-7650, AMT40, Germany) with an attachment for energy-dispersive X-ray (EDX) analysis for element mapping. The surface chemical composition of the samples was analysed by Fourier transform infrared (FTIR) spectroscopy (NICOLET 5700, Thermo Electron, USA). The order of their graphitic structures was examined by Raman spectroscopy (514 nm) (LabRAM HR Evolution, HORIBA Scientific, France) and the surface charged condition by zeta potential analysis (ZEN 3700 Zetasizer, Malvern, UK). Before the zeta potential measurement, samples were prepared in Milli-Q water at a concentration of 0.5 g L^{-1}. The suspension was adjusted to a pH range of 1 to 11 using NaOH or HCl solution and then sonicated for 30 min.

2.3 Experimental procedure

The kinetics of EDCs degradation were investigated using a pseudo-first-order model ($ln\frac{C_t}{C_0} = -kt$), which allows better comparison of reaction constants (k, min^{-1}) under different conditions. The error in the selected pollutant degradation rate constant was estimated from the scatter of the experimental data about the fitting line.

2.4 Quantification of chemical species

Prior to analysis, each sample (2 mL) was basified with 1 M NaOH (1 mL, pH ≈ 11) and filtered through a 0.45 μm polytetrafluoroethylene syringe filter to desorb BPA so as to separate the adsorption and degradation processes. This allowed us to determine the actual degradation of BPA during the experiment.

The concentrations of BPA, E2, and EE2 during kinetic experiments were determined by high-performance liquid chromatography (HPLC). The experiments were performed with UV detection at 277 nm. A flow rate of 1 mL min^{-1} was used with, as mobile phase, a mixture of water and methanol (30:70, v/v). A Nucleodur 100-5 C18 column with dimensions of 250 mm×4.6 mm was used. The retention time of BPA was 4 min. For determination of three EDCs (BPA, E2 and EE2) in different water samples, the fluorescence detector settings were λ_{ex} = 280 nm and λ_{em} = 305 nm. The mobile phase for isocratic elution comprised water and acetonitrile 50/50 (v/v) with a flow rate of 1 mL min^{-1}. Under these conditions, the retention times of BPA, E2, and EE2 were 4.9, 7.1 and 7.6 min, respectively. By-products derived from BPA were determined by ultra-high-performance liquid chromatography coupled to mass spectrometry (UHPLC-MS) and Ion Chromatography-Mass spectrometry (IC-MS). More details are provided in the Supplementary Material.

Electron spin resonance (ESR) experiments were performed on a JES-X320 spectrometer. DMPO (100 mM) was used as a radical probe for $SO_4^{\bullet-}$ and $^{\bullet}OH$. ESR spectra were registered at room temperature under the following operating conditions: modulation frequency 100 kHz, sweep width 0.5 mT, microwave power 1 mW, microwave frequency 9.15 GHz, and center field at 326.0 ± 5 mT.

3. Results and discussion

3.1 Material characterization

XRD patterns of GC-nZVI with different iron contents and pure ZVI are presented in Fig. S2a. With increasing Fe proportion ($[Fe]/[C]_n$), the signals at $2\theta = 44.7°$, 65.0°, and 82.4°, which are corresponded to the peak of pure ZVI, attributable to the (110), (200), and (211) planes of metallic iron, respectively (JCPDS No. 06-0696), gradually intensified. Further peaks at 43.7° and 50.9° correspond to the Fe_3C (JCPDS No. 03-0400). The formation of Fe_3C was mainly due to the reduction of pyrocarbon at high temperatures. However, the peak of GC could not be observed due to the strong signal peak of zero-valent iron. After removing the iron from the GC-nZVI using hydrochloric acid, there was a obvious signal peak at $2\theta = 26°$, which can be thought of as graphite crystal diffraction peak (JCPDS No. 26-1097). As given in the Raman spectra (Fig. S3), the G bands and D bands were found in the sample, as a feature of graphitized materials. And the ratio of the intensity of the D-band to the G-band (I_D/I_G), is also shown in the graph, and it can be seen that the GC-0.10-GC-nZVI has the smallest ratio of the three catalysts, indicating that it has the least amount of defective carbon and the highest degree of graphitization.

The derived textural properties were calculated by non-local density functional theory function of SAIEUS software and compiled in Table S1 (the specific nitrogen adsorption and desorption isotherms of the samples and pore size distributions are shown in Fig. S4). With the increase of Fe proportion, S_{BET} and the micropore and mesopore volume decreased. This could be attributed to the adsorption of ZVI on the carrier GC resulting in the blockage of the pores. It follows that the ZVI particles were not accumulated on the surface of the carbon but dispersed in its pores (Lv et al., 2011; Zhu et al., 2009). SEM image (Fig. S5) also clearly showed that at low iron loading, the iron was preferentially dispersed in the pores of the carbon rather than on the surface, spreading to the surface of the carbon when the iron was overloaded. In contrast, when there was no carbon carrier (Fig. S5d), the ZVI tends to gather together and has a larger particle size. The corresponding EDS elemental mappings (Fig. S6a–d) clearly illustrate the homogeneous distributions of C, O, and Fe in the samples. The presence of O may be due to the formation of iron oxide on the surface of the sample in contact with O_2 in the air. Moreover, the TEM image (Fig. S7a, b) revealed that ZVI in the material was evenly dispersed on the carbon, which had a typical graphitized structure, facilitating the transfer of photogenerated electrons (Wang et al., 2019b; Zhuang et al., 2017)

From the infrared spectrum of GC-nZVI in Figure S8, it can be seen that the sharp absorption peak near 3436 cm^{-1} was caused by the stretching vibration of -OH in the supported iron compound. At the same time, there was a strong absorption peak near 1630 cm^{-1}, which was formed by the

C=C stretching vibration of alkenes, and the peak at 1380 cm^{-1} was formed by the C-H deformation vibration of alkanes and alkenes. The peak at 1100 cm^{-1} was assigned to the C–O groups; the characteristic peak at 584 cm^{-1} was the Fe-O stretching vibration peak corresponding to Fe-O-H, which further verifies nZVI successfully loaded on carbon (Su et al., 2016). The zeta potential of the particles reflected the variation of surface charge with pH in aqueous solutions of different acidity (Fig. S9). The zero point of charge (pHzpc) of 0.05-GC-nZVI, 0.07-GC-nZVI and 0.10-GC-nZVI was observed at 3.25, 6.21 and 7.62, which were consistent with the results of previous studies(Wang et al., 2019a) (Ren et al., 2021). The loaded iron significantly reduces the specific surface area and hydrophobicity of the carbon. To investigate the impact of the loaded iron on reactivity, batch experiments were conducted.

3.2 Degradation of BPA using GC-nZVI with PS or PMS

The activation of PS and PMS by 0.07-GC-nZVI was investigated through assessing the efficiency of BPA degradation under different conditions. In the first step, BPA adsorption on 0.07-GC-nZVI, AC and GC were tested at pH 7 (Fig. S10a). From the kinetic results it was clear that the adsorption efficiency of GC was higher compared to AC. This was due to that the mesopore volume of GC was larger than that of AC, which was more conducive to the dispersion of BPA in the pore, as well as the high graphitisation of GC which facilitates the π-π interaction with the organics. The decrease in adsorption efficiency of 0.07-GC-nZVI was due to iron blocking the pore structure of GC, resulting in a decrease in the specific surface area of GC. But the data after desorption of the three indicated that the material itself had no degradation effect on BPA. But it can be observed that the adsorption was very fast, almost reaching equilibrium within 30 min. Therefore, the dark reaction adsorption time in subsequent experiments was set at 30 min.

In order to correlate the effect of iron doping amount to the degradation of BPA in the presence of PMS, a series of experiments was carried out as shown in Fig. S11. BPA was completely degraded within 30 min in the presence of GC-nZVI ($[Fe]/[C]_n$ = 0.07) and PMS, while BPA removal efficiencies of 47% and 85% within 30 min were achieved with $[Fe]/[C]_n$ 0.05 and 0.10, respectively. The results implied that an Fe to C ratio of 0.07 was optimal for BPA degradation.

To further optimize the BPA degradation efficiency of 0.07-GC-nZVI, the effects of pH and oxidant concentration were investigated. As shown in Fig. S12, 0.07-GC-nZVI showed good degradation efficiency as the pH was increased from 3 to 7. Under pH 3–7, most of the BPA was in uncharged forms (Yan et al., 2019b). No effect of pH on BPA removal towards 0.07-GC-nZVI composites may be attributed to no change in BPA species and surface charge of GC-nZVI (Fig. S9). At a PMS concentration of 0.1 mM, the degradation efficiency reached 100% within 60 min. When the PMS concentration was increased from 0.25 to 1.0 mM, the time for complete removal of BPA was shortened to less than 30 min. Considering the cost and the fact that the pH of actual environmental water is near-neutral, the conditions used in the subsequent experiments were 0.07-GC-nZVI at pH_0 = 7 and an oxidant concentration of 0.25 mM.

In the PMS or PS systems under dark conditions (Fig. S13), BPA was slowly degraded by the added ZVI after 60 min of treatment (20% with PMS, 15% with PS). In contrast, in the 0.07-GC-nZVI/PS or 0.07-GC-nZVI/PMS systems, significant increases in removal efficiency were observed, with complete removal of BPA within 45 min. And under UVA irradiation, without the addition of catalysts and oxidants, there is no degradation effect on BPA. Blank experiments showed that at most no BPA degradation was observed when PS and PMS used with or without UVA irradiation, confirming the catalytic effect of 0.07-GC-nZVI. To confirm the role of GC in the degradation effect of the catalyst, the removal and degradation effects of GC in different systems were compared (Fig. S10b) and the results showed that the addition of oxidants or UVA irradiation had little or no contribution to the removal of BPA. The data after desorption showed that the addition of PS or PMS to the system only improved the degradation by about 5%, and then only by 8% after the addition of UVA. This suggests that the use of GC alone as a catalyst does not improve the degradation of BPA. The BPA degradation constant (k, min^{-1}) (Fig 1c) increases considerably in the presence of GC-nZVI with the two oxidants (Fig. 1). Furthermore, in contrast to the system with PS, the use of UVA radiation using PMS accelerates the degradation of BPA from 0.185 min^{-1} to 0.261 min^{-1}. This synergistic effect indicates the contribution of a photo-induced process that increases the production of oxidizing species.

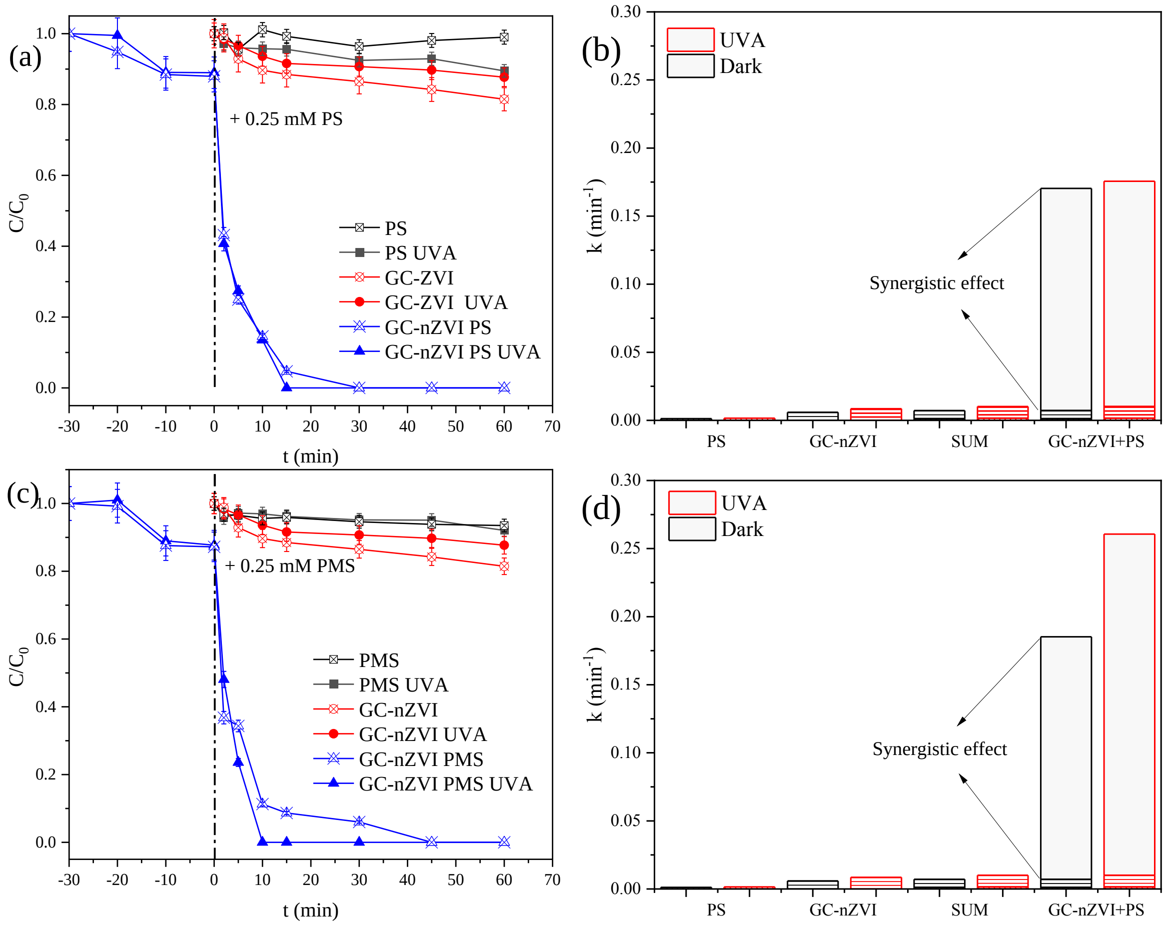

Fig. 1. BPA degradation efficiencies in different systems: (a) PS system, (b) PMS system and initial reaction rate constant in 10 min (c). Initial conditions: [BPA] = 25 µM, [PS] = [PMS] = 0.25 mM, [catalyst] = 0.05 g L^{-1}, pH$_0$ = 7.0 ± 0.1.

The catalytic ability of 0.07-GC-nZVI in different systems was also investigated. The introduction of UVA in the 0.07-GC-nZVI/PS system (Fig. 1a) accelerated the BPA degradation such that 100% degradation of BPA was achieved within 15 min instead of 30 min. A marked effect was also observed in the ZVI/PS system, with BPA degradation increasing from 15% to 56% after 1 h. The introduction of UVA to the 0.07-GC-nZVI/PMS system (Fig. 1b) significantly reduced the reaction time for complete degradation of BPA from 45 min to 10 min. Thus, it is clear that the introduction of UVA promotes the generation of radicals, providing insight into the mechanism in these two systems.

3.3 Contributions of free radicals in different systems

The contributions of radical species in the degradation of BPA were determined through quenching experiments. Typically, PMS / PS generate $SO_4^{\bullet-}$ and $^{\bullet}OH$ during the activation process. At an appropriate concentration, isopropanol (Isop) can effectively quench $SO_4^{\bullet-}$ and $^{\bullet}OH$ with second-order rate constants of $k_{\mathrm{Isop},SO_4^{\bullet-}} = 8.2 \times 10^7\ \mathrm{M}^{-1}\ \mathrm{s}^{-1}$ and $k_{\mathrm{isop},\ ^{\bullet}OH} = 1.9 \times 10^9\ \mathrm{M}^{-1}\ \mathrm{s}^{-1}$, whereas *tert*-butanol (TBA) can only quench $^{\bullet}OH$ ($k_{\mathrm{TBA},\ ^{\bullet}OH} = 6.0 \times 10^8\ \mathrm{M}^{-1}\ \mathrm{s}^{-1}$; $k_{\mathrm{TBA},SO_4^{\bullet-}} = 8.3 \times 10^5\ \mathrm{M}^{-1}\ \mathrm{s}^{-1}$) (Buxton et al., 1988; Huie et al., 1991). In the system 0.07-GC-nZVI + PS, the addition of 5 mM TBA had almost no effect on BPA degradation, whereas in the presence of 40 mM Isop, up to 62% inhibition was observed after 60 min of reaction (Fig. S14a). A similar trend was observed under UVA irradiation, whereby inhibition by Isop was about 45% (Fig. S14b). When 0.25 mM PMS was used in the dark and under UVA irradiation, negligible effect on BPA removal was observed in the presence of TBA (5 mM), whereas the BPA degradation efficiency was inhibited by about 60% within 60 min under both dark and light conditions in the presence of Isop.

BPA degradation rate constants (k, min^{-1}) over the first 10 min in different reaction systems are indicated in Fig. 2. In the presence of PS, the use of UVA led to an increase in k from 0.170 to 0.176 min^{-1}. In the presence of TBA, k was reduced by only about 7% (0.158 min^{-1} in the dark; 0.167 min^{-1} under UVA), further indicating that $^{\bullet}OH$ was not dominant in the reaction. In the presence of Isop, k decreased to 0.056 and 0.026 min^{-1}, respectively. A similar trend was observed when PMS was used, whereby the addition of Isop to the 0.07-GC-nZVI/PMS/UVA system led to a decrease in k from 0.261 to 0.051 min^{-1}. These findings suggest that the principal radical involved in the activation of PMS and PS by 0.07-GC-nZVI is $SO_4^{\bullet-}$. It is also evident that UVA irradiation increases the BPA degradation rate constant by promoting the generation of radicals, consistent with the results reported in Figure 1. In some paper, the formation of singlet oxygen trough reactivity of iron with PS or PMS has been reported. In order to clarify this point, furfuryl alcohol (FFA) was used as a quencher, which was due to its reactivity with $^1O_2$ in addition to the also well know reactivities with $HO^\bullet$ and $SO_4^{\bullet-}$. By comparing the quenching effects when FFA (0.5 mM) was used alone or in the presence of ISOP (40 mM) (see Fig. S15), we can see that no difference was determined, indicating that no $^1O_2$ was produced in this system.

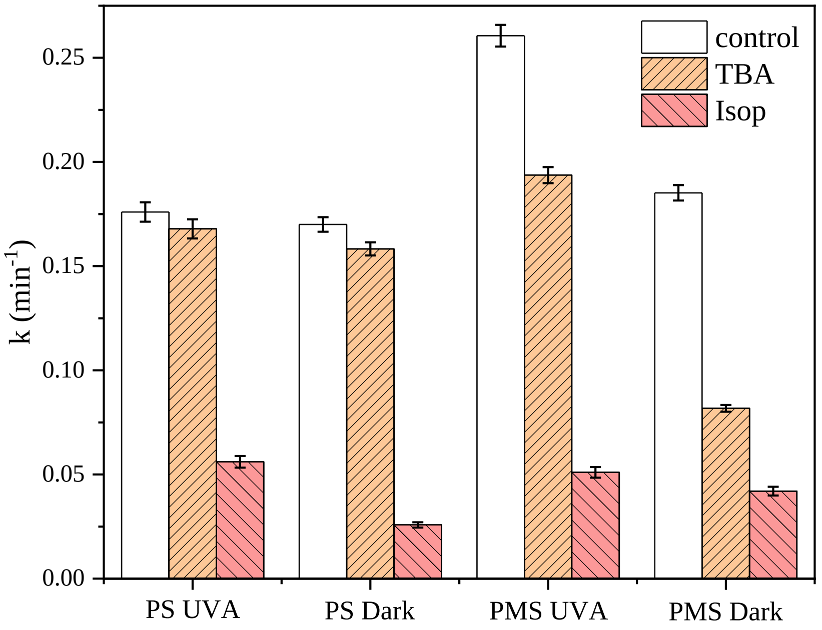

Fig. 2. Effects of TBA and Isop on the degradation rate constants of BPA in different systems. Initial conditions: [PS] = [PMS] = 0.25 mM, [catalyst] = 0.05 g L^{-1}, [TBA] = 5 mM, [Isop] = 40 mM, $pH_0 = 7.0 \pm 0.1$.

3.4 High-valent Iron species

The addition of Isop did not completely inhibit the degradation of BPA, suggesting that other reactive species besides $^{\bullet}OH$ and $SO_4^{\bullet-}$ were also generated. The formation of high-valent iron in heterogeneous Fenton and Fenton-like processes has been reported in different works (Farinelli et al., 2020; Litter andSlodowicz, 2017). PMSO has been reported as a chemical probe for ferryl ions ($Fe^{IV}O^{2+}$) giving $PMSO_2$ as a product. Through an oxygen atom transfer mechanism, sulfoxide is readily oxidized to the corresponding sulfone by high-valence metal oxygen species which differs from the $SO_4^{\bullet-}$ and $^{\bullet}OH$ mediated pathways. In order to assess whether the high-valent metal oxide species [Fe^{IV}] were produced in the different systems, the production of $PMSO_2$ by selective oxidation of PMSO was determined. As shown in Figure 3a, in the GC-nZVI/PS system, 57 µM PMSO was oxidized after 30 min, and 26 µM $PMSO_2$ was produced. And after the addition of UVA irradiation, 72 µM PMSO was oxidized and 27 µM $PMSO_2$ was produced.

Blank experiments showed neither degradation of PMSO nor production of $PMSO_2$ in the presence of PS alone, with or without UVA irradiation, indicating that PS alone could not react with PMSO. In the PMS system (Figure 3b), some oxidation of PMSO was observed with the production of $PMSO_2$. However, by calculating the percentage of [$PMSO_2$] to $[PMSO]_0$, it transpired that 3% and 4% of $PMSO_2$ were produced in the dark and light reactions, respectively, with corresponding increases of 7% and 9% upon the addition of catalyst, suggesting a direct contribution of Fe^{IV} in the PMS system. Thus, BPA degradation is not only attributable to radicals, but also to Fe^{IV}, and we can argue that exposure to UVA promotes the degradation of PMSO and the generation of $PMSO_2$, suggesting that the positive effect of UVA on BPA degradation is due to both the promotion of radical production and Fe^{IV}.

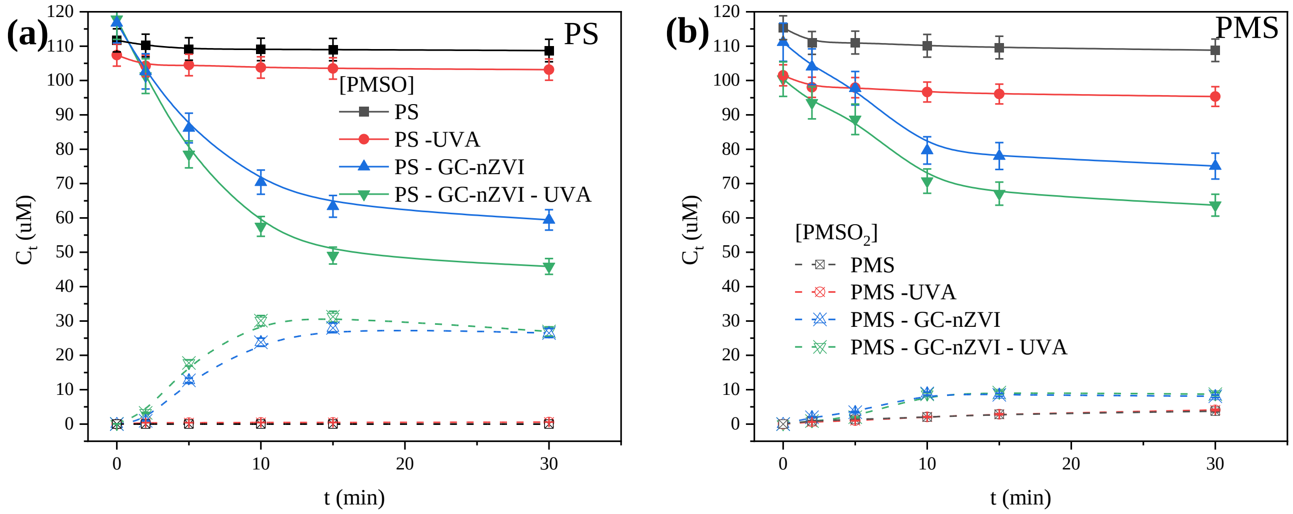

Fig. 3. PMSO degradation and $PMSO_2$ formation in (a) PS system and (b) PMS system, [PS] = [PMS] = 0.25 mM, [catalyst] = 0.05 g L^{-1}, $pH_0 = 7.0 \pm 0.1$.

3.5 Steady state concentrations of reactive species

In order to determine the steady-state concentrations of each reactive species in the various systems, a kinetic approach under different experimental conditions in the presence of PMSO and TBA was employed. The first simplified step is the generation of $^{\bullet}OH$, $SO_4^{\bullet -}$, and $Fe^{IV}O^{2+}$ through the reaction of GC-nZVI with PS and PMS (R1). PMSO was used due to its reactivity with all reactive species (R2−R4) and to quantify the generation of $Fe^{IV}O^{2+}$ in solution through the selective formation of $PMSO_2$ (R4) while TBA was used as a selective $^{\bullet}OH$ scavenger (R5).

GC-nZVI + PS/PMS → $^{\bullet}OH + SO_4^{\bullet -} + Fe^{IV}O^{2+}$ (R1)

$^{\bullet}OH$ + PMSO → products k_2 (R2)

$SO_4^{\bullet -}$ + PMSO → products k_3 (R3)

$Fe^{IV}O^{2+}$ + PMSO → Fe^{2+} + $PMSO_2$ k_4 (R4)

$^{\bullet}OH$ + TBA → products k_5 (R5)

Considering the rate constants of reactions between TBA and oxidant species such as $^{\bullet}OH$, $SO_4^{\bullet -}$, and $Fe^{IV}O^{2+}$ (6.0×10^8, 8.4×10^5 and × 6.0×10^1 M^{-1} s^{-1}), (Bakac et al., 2004; Buxton et al., 1988; Neta et al., 1996) we can argue that 5 mM TBA is sufficient to selectively scavenge all generated $^{\bullet}$OH, while its effects on $SO_4^{\bullet -}$ and $Fe^{IV}O^{2+}$ are negligible.

The results presented in figure S16 show that the addition of 5 mM TBA partially inhibited the degradation of PMSO when 0.07-GC-nZVI (0.05 g L^{-1}) was used in the presence of 0.25 mM PS, decreasing the degradation rates of PMSO from 7.57×10^{-8} M s^{-1} and 9.96×10^{-8} M s^{-1} in the dark and under UVA to 5.82×10^{-8} M s^{-1} and 6.11×10^{-8} M s^{-1}, respectively. A similar effect was observed when PMS was used, with decreases in the PMSO degradation rates from 5.14×10^{-8} M s^{-1} and 3.87×10^{-8} M s^{-1} to 3.84×10^{-8} M s^{-1} and 2.28×10^{-8} M s^{-1}, respectively.

It can be concluded that, under the adopted conditions, the degradation of PMSO is due to the combined effects of R3 and R4, as expressed by Eq. (1) (Fig. S16), where $\frac{d[PMSO]}{dt}$ is the degradation rate of PMSO (M s^{-1}), and k_3 and k_4 are the second-order rate constants for reactions between PMSO and $SO_4^{\bullet -}$ and $Fe^{IV}O^{2+}$, respectively.

$$\frac{d[PMSO]}{dt} = -k_3[PMSO][SO_4^{\bullet -}]_{ss} - k_4[PMSO][Fe^{IV}O^{2+}]_{ss} \qquad (1)$$

The formation of $PMSO_2$ depends only on $Fe^{IV}O^{2+}$ and can be modelled according to Eq. (2)

$$\frac{d[PMSO_2]}{dt} = k_4[PMSO][Fe^{IV}O^{2+}]_{ss} \qquad (2)$$

The steady state concentration of $Fe^{IV}O^{2+}$ ($[Fe^{IV}O^{2+}]_{ss}$) can then be calculated from Eq. (2) by plotting the formation of $PMSO_2$ during the reaction period and considering the initial PMSO concentration of 100 µM and $k_4 = 1.23 \times 10^5$ M^{-1} s^{-1} (Pestovsky andBakac, 2006). This value has used to determine $[SO_4^{\bullet -}]_{ss}$ from Eq. (1). Finally, $[Fe^{IV}O^{2+}]_{ss}$ and $[SO_4^{\bullet -}]_{ss}$ were used to calculate $[HO^{\bullet}]_{ss}$ according to Eq. (3) by plotting PMSO degradation without TBA.

$$\frac{d[PMSO]}{dt} = -k_2[PMSO][HO^{\bullet}]_{ss} - k_3[PMSO][SO_4^{\bullet -}]_{ss} - k_4[PMSO][Fe^{IV}O^{2+}]_{ss} \qquad (3)$$

The steady state concentrations of each reactive species generated in the presence of PS and PMS in the dark and under UVA irradiation are given in Table 2

Table 2. The concentrations of each reactive species generated in the presence of PS and PMS iin

the dark and under UVA irradiation

	PS		***PMS***	
	Dark	Irradiation	Dark	Irradiation
$[\mathbf{HO^{\bullet}}]_{\mathbf{ss}}$ $(\mathbf{M})$	4.60×10^{-14}	9.39×10^{-14}	3.36×10^{-14}	5.07×10^{-14}
$[\mathbf{SO_4^{\bullet-}}]_{\mathbf{ss}}$ $(\mathbf{M})$	5.15×10^{-13}	1.57×10^{-13}	7.45×10^{-13}	4.59×10^{-13}
$[\mathbf{Fe^{IV}O^{2+}}]_{\mathbf{ss}}$ $(\mathbf{M})$	2.59×10^{-9}	3.71×10^{-9}	8.52×10^{-10}	4.64×10^{-10}

We also used EPR spectroscopy to detect variations in different reactive oxygen species (ROS) contents in the GC-nZVI/PS and GC-nZVI/PMS systems. When DMPO was used as a trapping agent, peaks due to DMPO−OH and DMPO-SO_4^- could be detected but without DMPO−O_2^-, as shown in Fig. S17. However, in contrast to the quenching experiments, the signal intensity of $SO_4^{\bullet-}$ was lower than that of $^{\bullet}OH$, which might be attributed to the much lower rate constant of the reaction between DMPO and $SO_4^{\bullet-}$ ($k = 2.9 \times 10^4$ M^{-1} s^{-1}) compared to that of the reaction between DMPO and $^{\bullet}OH$ ($k = 2.8 \times 10^9$ M^{-1} s^{-1}) (Wei et al., 2017). When TEMP was used as a trapping agent (Fig. S18), no change in the ESR signal when only TEMP of TEMP + PS + GC-nZVI was measured after 2 min of acquisition. So, we prove that there is no singlet oxygen in our experimental system.

3.6 BPA degradation products and mineralization efficiency

In this study, BPA ($[M+H]^+$, *m*/z 299.1254) degradation products in the 0.07GC-nZVI + PS or PMS systems were determined by LC-MS. Different compounds were identified based on m/z values. A first class of different hydroxylated products generated from the attack of oxidant species ($^{\bullet}OH$, $SO_4^{\bullet-}$, and probably $Fe^{IV}O^{2+}$) on the aromatic ring, forming a cyclohexadienyl radical rapidly, were rapidly oxidized to hydroxylated derivatives such as P1 (monohydroxylated BPA; $[M–H]^-$, *m/z* 243.0367), P2 (dihydroxylated BPA; $[M+H]^+$, *m/z* 261.0110), and P3 (trihydroxylated BPA;

$[M\text{+H}]^+$, *m*/*z* 277.1695) when PS and PMS were used as oxidant precursors. Further oxidation of hydroxylated products generated P4 ($[M\text{+H}]^+$, *m*/*z* 244.1906) and P5 ($[M\text{–H}]^-$, *m*/*z* 241.0573). Finally, aromatic ring-opening furnished P6 ($[M\text{–H}]^-$, *m*/*z* 277.1091), P7 ($[M\text{–H}]^-$, *m*/*z* 275.1696), P8 ($[M\text{–H}]^-$, *m*/*z* 205.0899), and P9 ($[M\text{–H}]^-$, *m*/*z* 137.0234). (Fig. 4).

Efficient oxidation of organic molecules leads to the formation of short chain carboxylic acids (CAs) before complete mineralization. We used IC-MS analysis to identify the main CAs generated during BPA degradation using 0.07-GC-nZVI/PS/UVA. In order to improve the formation of CAs, we increased the concentrations of all reactants in the solution (100 µM BPA, 0.2 g L^{-1} GC-nZVI and 1 mM PMS). IC-MS results (Fig. S19a), indicated that intermediates such as oxalate, formate, acetate, and propane-1,2,3-triol were generated during the reaction. As can be seen in Fig. S19b, about 10 µM acetate and 100 µM formate were produced after the reaction had proceeded for 79 h, while the concentration of oxalate was immeasurably low. However, it is interesting to note that oxalic acids, which is able to complex iron in solution to generate a photolabile iron-oxalate complex, first accumulated and was then slowly degraded in the solution, implicating it as a BPA degradation product during GC-nZVI/PS/UVA activation.

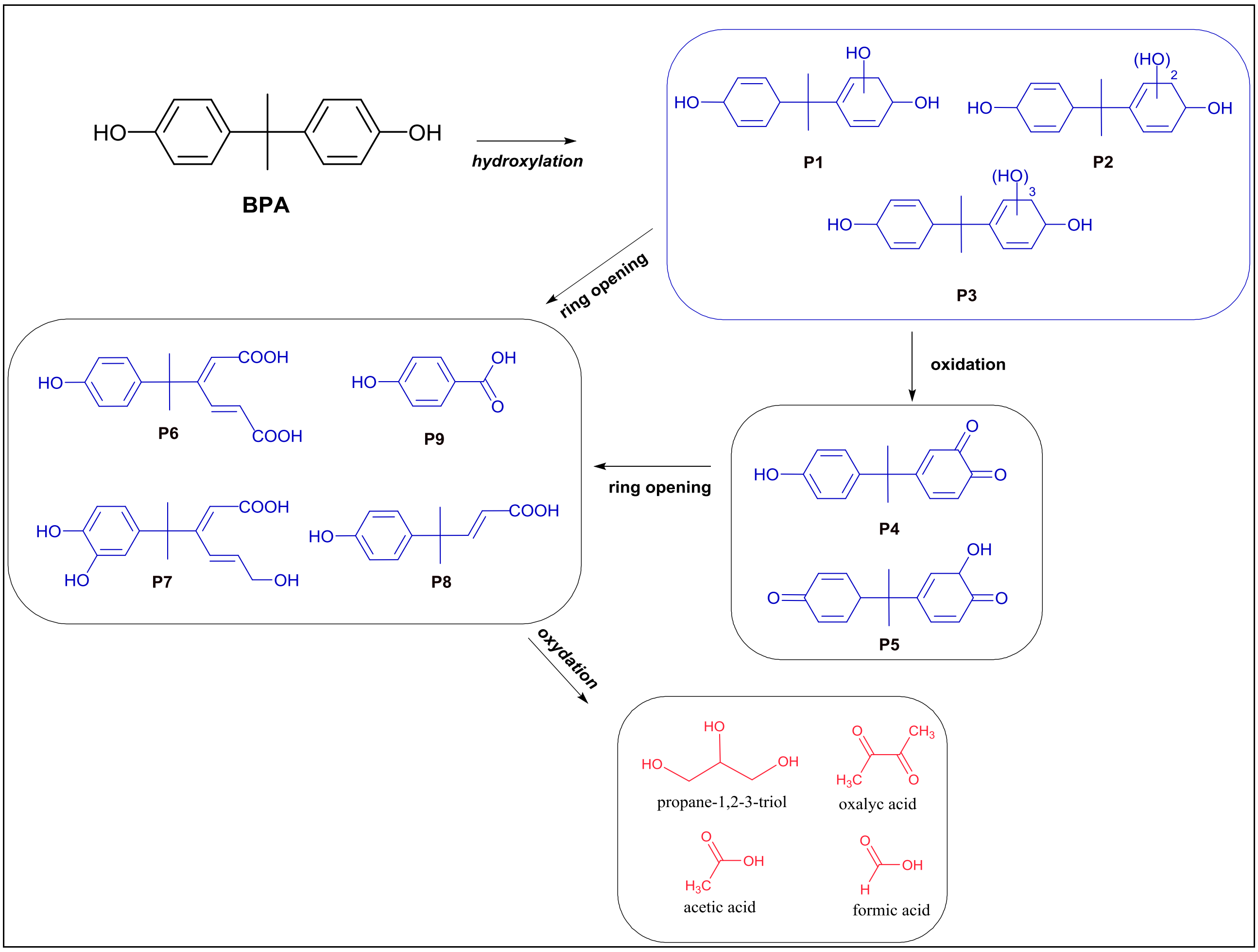

Fig. 4: Suggested pathways of BPA degradation based on the LC-MS (blue) and IC-MS (red) analyses.

Total organic carbon (TOC) analysis was used as a measure of mineralization efficiency in our systems. Mineralization of BPA by 0.07-GC-nZVI catalyzed by PMS and PS were compared (Fig. 5). Both systems fully degraded BPA within 30 min, while up to 80% mineralization was achieved after 2 h, showing good efficiency of our process for the degradation and mineralization of BPA compared to other catalytic oxidation systems based on PMS or PS.

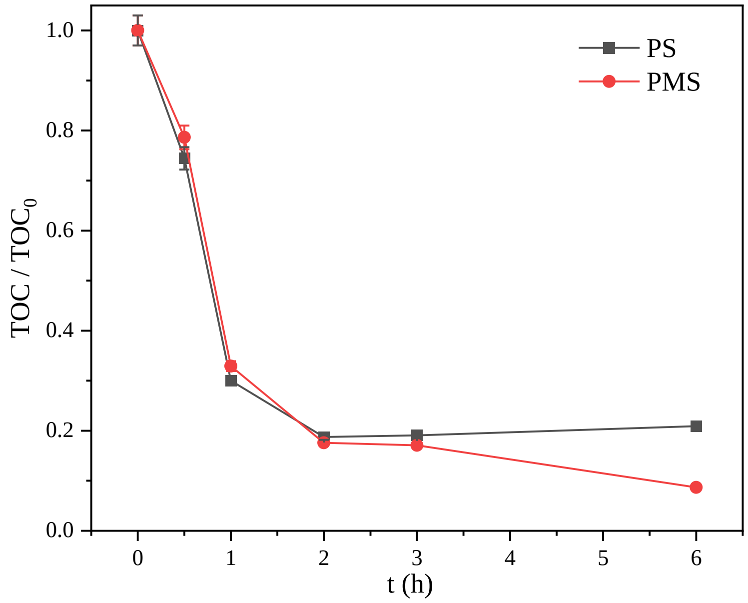

Fig. 5. TOC tests of GC-nZVI. Initial conditions: [BPA] = 25 µM, [PS] = [PMS] = 0.25 mM, [catalyst] = 0.05 g L^{-1}, pH$_0$ = 7.0 ± 0.1, UVA.

3.7 Recyclability and Suitability of GC-nZVI in PMS/PS activation

Catalyst stability is an important property for practical applications. For its assessment, we used twofold higher concentrations of each species in solution. Rrecycling experiments in this study were performed by directly adding fresh BPA and PS/PMS to the reaction solution for multiple runs. As shown in Figure 6, a slight decrease in degradation efficiency was observed in the second and third runs. This trend can be explained by considering different factors arisring during the experimental procedure. (i) We did not wash the sample and add again PS/PMS during the cycle; only BPA was added to re-establish an initial concentration of 50 µM. Moreover, BPA by-products in the solution may play a competitive role in the oxidation of BPA. (ii) The GC-nZVI concentration decreased with each cycle. This problem was partially circumvented by increasing the initial GC-nZVI concentration. However, a loss of catalyst was incurred when samples were withdrawn for analysis. (iii) During each cycle, a fixed volume of BPA solution was added, resulting in an additional dilution of PS/PMS and GC-nZVI. Despite this, a removal efficiency of

70% was maintained after three runs at 60 min, indicating good stability and reusability of 0.07-GC-nZVI.

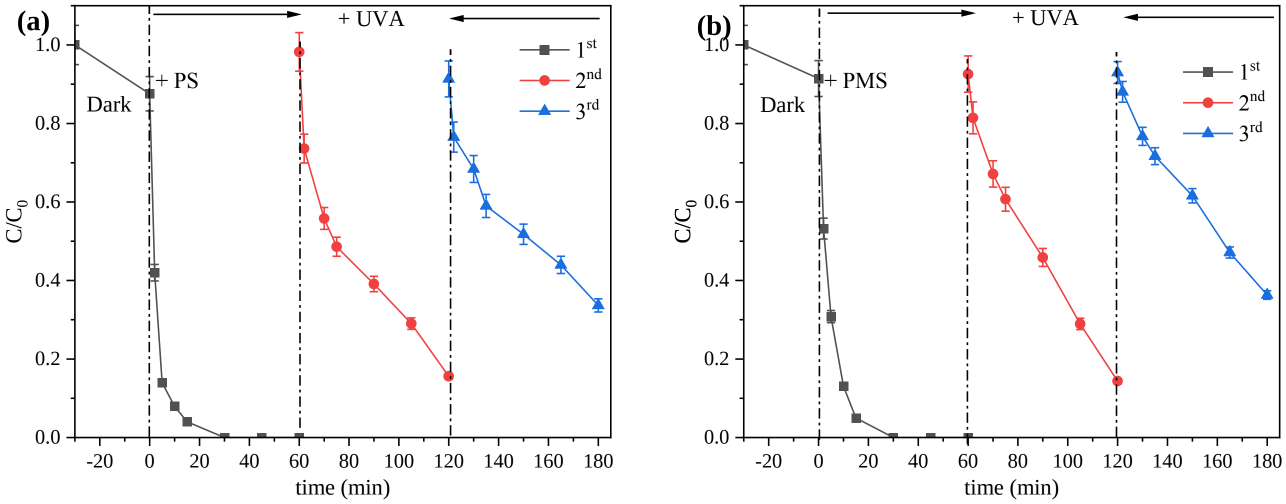

Fig. 6. Reusability tests of GC-nZVI. Initial conditions: $[BPA]_0$ = 50 μM, [PS] = $[PMS]_0$ = 0.5 mM, [catalyst] = 0.1 g L^{-1}, pH_0 = 7.0 ± 0.1.

As shown in Fig. S2c, comparing the XRD patterns before and after reactions in the PS and PMS systems, it can be seen that the peak due to ZVI ($2\theta = 44.7°$) was significantly weakened, which indicates that Fe showed a certain degree of dissolution during the reaction process. Nevertheless, SEM and TEM images showed that the structure of the sample was not destroyed, confirming the stability of the material (Figs. S6e, f and S7c, d). The FITR spectrum after the reaction can see that the fluctuation at 1100 cm^{-1} was weakened, and the wavenumber at 584 cm^{-1} was changed, which may be because the dissolution of iron affects the bonding effects between ZVI and carbon (Yan et al., 2015).

XPS patterns clearly showed the presence of C, O, and Fe in both samples (Fig. S20a). The O content of used GC-nZVI in the PS/PMS systems increased sharply to 23.8% and 25.9%, respectively, as compared to 6.2% in the fresh GC-nZVI, which was presumably due to the oxidation of Fe. Fe 2p core-level spectra (Fig. S20b–d) of the GC-nZVI indicated the presence of

Fe^0 (708.6 eV), Fe^{2+} (710.5 eV), and Fe^{3+} (711.6 and 713.2 eV) (Jiang et al., 2019). These results indicate that part of the ZVI on the carbon surface was oxidized to Fe^{3+} and Fe^{2+} when exposed to air, resulting in an attenuation of its peak (Zhang andShen, 2020). After the reaction, the atom Fe^0 were oxidized and lost. However, it can be seen from the XRD results that this did not lead to complete oxidation or dissolution of the ZVI in the material, but only a relative oxidation.

Inorganic anions and natural organic matter (NOM) are ubiquitous in the aqueous environment, and also have significant impacts on the performance of AOPs. They can react with free radicals, thus influencing the type and concentration of active species and leading to variations in the removal efficiencies of target organic pollutants. As can be seen in Figure S21, different concentrations of chloride ions (Cl^-) had no inhibitory effect on the degradation of BPA in the different systems. However, high concentrations of hydrogen carbonate ions (HCO_3^-) exerted a significant negative effect on the removal efficiency, as can be seen in Figure S22, although the degradation of BPA did not decrease further when the HCO_3^- concentration was increased from 2 to 5 mM. This suggests that $^{\bullet}OH$ and $SO_4^{\bullet-}$ produced in our system react with HCO_3^- to form weak redox radical species [as expressed by reactions (6) and (7)]. .

$$^{\bullet}OH + HCO_3^- \rightarrow HCO_3^{\bullet} + OH^- \qquad 8.5 \times 10^6\ \mathrm{M^{-1}\ s^{-1}} \qquad \text{(R6)}$$

$$SO_4^{\bullet-} + HCO_3^- \rightarrow HCO_3^{\bullet} + SO_4^{2-} \qquad 9.1 \times 10^6\ \mathrm{M^{-1}\ s^{-1}} \qquad \text{(R7)}$$

NOM in surface water is often considered to be a scavenger, leading to a reduction in the degradation efficiency of target pollutants by competing with ROS in AOPs. Therefore, as a representative of NOM, humic acid (HA) was considered in BPA degradation. In Figure S23, an increase in HA concentration from 2 to $10\ \mathrm{mg_C}^{-1}$ is seen to have a negative impact on the efficiency of the degradation. At an HA concentration of $10\ \mathrm{mg_C\ L^{-1}}$, the BPA degradation rate constants (k) of different reaction systems (Figure S24) were greatly reduced to around $0.05\ \mathrm{min^{-1}}$, which may be attributed to competitive reactions of reactive species with HA and BPA.

The potential of GC-nZVI for practical application in PS and PMS systems was further investigated by the degradation of different pollutants (BPA, E2, and EE2) in different water samples (see Table S2 for detailed information on these water samples). The experiments were carried out in the same way as described for BPA degradation, with an initial concentration of 5 μM for all three pollutants.

As shown in Figure 7, the removal efficiencies in the different water sources were in the order: pure water > tap water > STPW. In pure water, 100% removal was achieved within 60 min with the addition of only 0.25 mM PS or PMS, which could be reduced to 15 min in the irradiated systems. In both tap water and STPW, it can be observed that the degradation process slowed down after the first addition of 0.25 mM PS/PMS after 30 min of reaction, but restarted with the addition of fresh PS/PMS. This suggested that the reduction in degradation efficiency in both water samples was due to the presence of inorganic or organic pollutants rapidly depleting the oxidant, and that better degradation can be achieved under conditions of sufficient oxidant, while the catalyst can be used continuously. The potential of 0.07-GC-nZVI for practical environmental remediation applications remains significant.

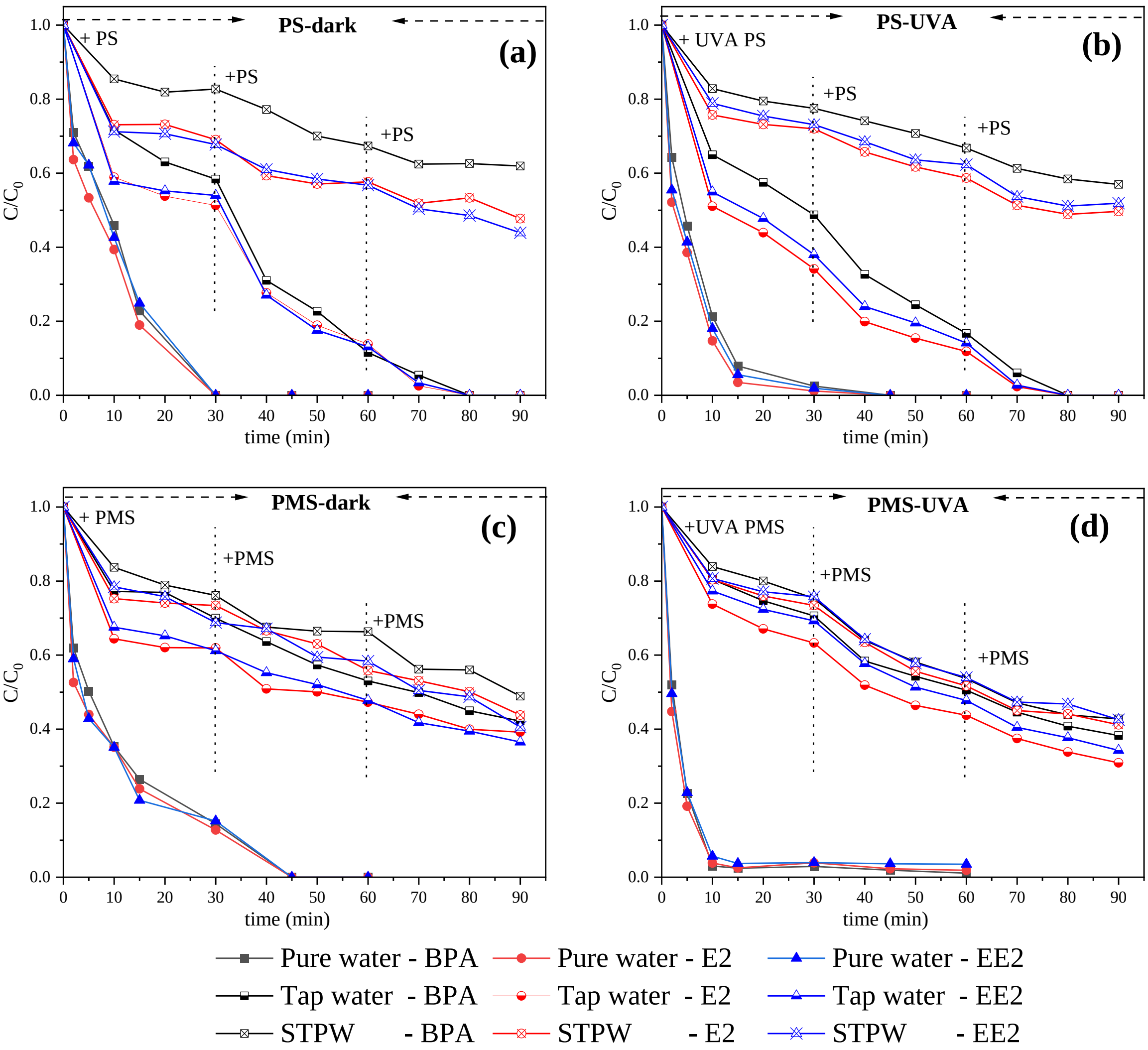

Fig. 7. Photocatalytic activities in organic compounds degradation by GC-nZVI in various water samples with different systems: [BPA] = [E2] = [EE2] = 5 μM, $[PS]_0$ = $[PMS]_0$ = 0.25 mM, [catalyst] = 0.05 g L^{-1}, pH_0 = 7.0 ± 0.1.

4. Conclusion

Nano zero-valent iron (nZVI) has been deposited on graphitized carbon (GC) to prepare catalysts suitable for environmental remediation. Of the prepared catalysts, 0.07-GC-nZVI exhibited high BPA removal efficiency in the presence of PMS or PS. BPA (25 μM) could be fully removed by 0.05 g L^{-1} 0.07-GC-nZVI in the presence of only 0.25 mM of PMS or PS within 30 min. Compared with pure ZVI, it can be seen that GC significantly enhances the adsorption of compounds at the active sites. Exposure to UVA irradiation slightly improves the degradation efficiency of BPA. Reactive species responsible for BPA degradation at near-neutral pH have been systematically identified. Our results imply that the 0.07-GC-nZVI/PMS or PS systems generate $SO_4^{\bullet-}$, $^{\bullet}OH$, and Fe(IV) at steady-state concentrations ranging from 3.4×10^{-14} to 3.7×10^{-9} M. Among them, $SO_4^{\bullet-}$ plays the dominant role in the degradation process. Moreover, 0.07-GC-nZVI also demonstrated good stability and efficiency during application in tap and STP water samples. This work provides new insight into heterogeneous Fenton and photo-Fenton catalytic degradation processes, which offer good practical application potential.

Acknowledgments

Authors acknowledge the Ministry of Education of China for providing the financial support for Minjuan CAI stay in France and PRC program CNRS/NSFC n°270437.

References

Ahmed, M.B., Zhou, J.L., Ngo, H.H., Guo, W., Thomaidis, N.S., Xu, J. 2017. Progress in the biological and chemical treatment technologies for emerging contaminant removal from wastewater: A critical review. *Journal of Hazardous Materials, 323*, 274-298.https://doi.org/10.1016/j.jhazmat.2016.04.045

Annamalai, J., Namasivayam, V. 2015. Endocrine disrupting chemicals in the atmosphere: Their effects on humans and wildlife. *Environment International, 76*, 78-97.https://doi.org/10.1016/j.envint.2014.12.006

Bakac, A., Shi, C., Pestovsky, O. 2004. Acid-Catalyzed Oxidation of Iodide Ions by Superoxo Complexes of Rhodium and Chromium. *Inorganic Chemistry, 43*, 5416-5421.10.1021/ic049629j

Buxton, G.V., Greenstock, C.L., Helman, W.P., Ross, A.B. 1988. Critical Review of rate constants for reactions of hydrated electrons, hydrogen atoms and hydroxyl radicals (·OH/·O[−] in Aqueous Solution. *Journal of Physical and Chemical Reference Data, 17*, 513-886.10.1063/1.555805

Chang, H.-S., Choo, K.-H., Lee, B., Choi, S.-J. 2009. The methods of identification, analysis, and removal of endocrine disrupting compounds (EDCs) in water. *Journal of Hazardous Materials, 172*, 1-12.https://doi.org/10.1016/j.jhazmat.2009.06.135

Chen, T., Fu, C., Liu, Y., Pan, F., Wu, F., You, Z., Li, J. 2021. Adsorption of volatile organic compounds by mesoporous graphitized carbon: Enhanced organophilicity, humidity resistance, and mass transfer. *Separation and Purification Technology, 264*, 118464.https://doi.org/10.1016/j.seppur.2021.118464

Esplugas, S., Bila, D.M., Krause, L.G.T., Dezotti, M. 2007. Ozonation and advanced oxidation technologies to remove endocrine disrupting chemicals (EDCs) and pharmaceuticals and personal care products (PPCPs) in water effluents. *Journal of Hazardous Materials, 149*, 631-642.https://doi.org/10.1016/j.jhazmat.2007.07.073

Farinelli, G., Minella, M., Pazzi, M., Giannakis, S., Pulgarin, C., Vione, D., Tiraferri, A. 2020. Natural iron ligands promote a metal-based oxidation mechanism for the Fenton reaction in water environments. *Journal of Hazardous Materials, 393*, 122413.https://doi.org/10.1016/j.jhazmat.2020.122413

Ghazal, H., Koumaki, E., Hoslett, J., Malamis, S., Katsou, E., Barcelo, D., Jouhara, H. 2022. Insights into current physical, chemical and hybrid technologies used for the treatment of wastewater contaminated with pharmaceuticals. *Journal of Cleaner Production, 361*, 132079.https://doi.org/10.1016/j.jclepro.2022.132079

Giannakis, S., Lin, K.-Y.A., Ghanbari, F. 2021. A review of the recent advances on the treatment of industrial wastewaters by Sulfate Radical-based Advanced Oxidation Processes (SR-AOPs). *Chemical Engineering Journal, 406*, 127083.https://doi.org/10.1016/j.cej.2020.127083

Giulivo, M., Lopez de Alda, M., Capri, E., Barceló, D. 2016. Human exposure to endocrine disrupting compounds: Their role in reproductive systems, metabolic syndrome and breast cancer. A review. *Environmental Research, 151*, 251-264.https://doi.org/10.1016/j.envres.2016.07.011

Gowrisankaran, S., Thrinavukkarasu, G.K., Hanif, M.B., Liapun, V., Roch, T., Satrapinskyy, L., Plesch, G., Motola, M., Monfort, O. (2022). Fe-Modified TiO2 Nanotube Layer as a Photochemically Versatile Material for the Degradation of Organic Pollutants in Water. In *Engineering Proceedings*, vol. 19).

Gujar, S.K., Divyapriya, G., Gogate, P.R., Nidheesh, P.V. 2023. Environmental applications of ultrasound activated persulfate/peroxymonosulfate oxidation process in combination with other activating agents. *Critical Reviews in Environmental Science and Technology, 53*, 802.10.1080/10643389.2022.2085965

Huie, R.E., Clifton, C.L., Neta, P. 1991. Electron transfer reaction rates and equilibria of the carbonate and sulfate radical anions. *International Journal of Radiation Applications and Instrumentation. Part C. Radiation Physics and Chemistry, 38*, 477-481.https://doi.org/10.1016/1359-0197(91)90065-A

Jia, D., Li, Q., Hanna, K., Mailhot, G., Brigante, M. 2021a. Efficient removal of estrogenic compounds in water by MnIII-activated peroxymonosulfate: Mechanisms and application in sewage treatment plant water. *Environmental Pollution, 288*, 117728.https://doi.org/10.1016/j.envpol.2021.117728

Jia, J., Wei, L., Li, F., Yu, C., Yang, K., Liang, T. 2021b. In situ growth of NiFe MOF/NF by controlling solvent mixtures as efficient electrocatalyst in oxygen evolution. *Inorganic Chemistry Communications, 128*, 108605.https://doi.org/10.1016/j.inoche.2021.108605

Jiang, S.-F., Ling, L.-L., Chen, W.-J., Liu, W.-J., Li, D.-C., Jiang, H. 2019. High efficient removal of bisphenol A in a peroxymonosulfate/iron functionalized biochar system: Mechanistic elucidation and quantification of the contributors. *Chemical Engineering Journal, 359*, 572-583.https://doi.org/10.1016/j.cej.2018.11.124

Kakavandi, B., Alavi, S., Ghanbari, F., Ahmadi, M. 2022. Bisphenol A degradation by peroxymonosulfate photo-activation coupled with carbon-based cobalt ferrite nanocomposite: Performance, upgrading synergy and mechanistic pathway. *Chemosphere, 287*, 132024.https://doi.org/10.1016/j.chemosphere.2021.132024

Khan, S., He, X., Khan, J.A., Khan, H.M., Boccelli, D.L., Dionysiou, D.D. 2017. Kinetics and mechanism of sulfate radical- and hydroxyl radical-induced degradation of highly chlorinated pesticide lindane in UV/peroxymonosulfate system. *Chemical Engineering Journal, 318*, 135-142.https://doi.org/10.1016/j.cej.2016.05.150

Kim, S., Eom, S., Kim, H.-J., Lee, J.J., Choi, G., Choi, S., Kim, S., Kim, S.Y., Cho, G., Kim, Y.D., Suh, E., Kim, S.K., Kim, S., Kim, G.-H., Moon, H.-B., Park, J., Kim, S., Choi, K., Eun, S.-H. 2018. Association between maternal exposure to major phthalates, heavy metals, and persistent organic pollutants, and the neurodevelopmental performances of their children at 1 to 2years of age- CHECK cohort study. *Science of The Total Environment, 624*, 377-384.https://doi.org/10.1016/j.scitotenv.2017.12.058

Kimura, K., Toshima, S., Amy, G., Watanabe, Y. 2004. Rejection of neutral endocrine disrupting compounds (EDCs) and pharmaceutical active compounds (PhACs) by RO membranes. *Journal of Membrane Science, 245*, 71-78.https://doi.org/10.1016/j.memsci.2004.07.018

Li, Y., Yang, T., Qiu, S., Lin, W., Yan, J., Fan, S., Zhou, Q. 2020. Uniform N-coordinated single-atomic iron sites dispersed in porous carbon framework to activate PMS for efficient BPA degradation via high-valent iron-oxo species. *Chemical Engineering Journal, 389*, 124382.https://doi.org/10.1016/j.cej.2020.124382

Lin, Z., Qin, W., Sun, L., Yuan, X., Xia, D. 2020. Kinetics and mechanism of sulfate radical- and hydroxyl radical-induced degradation of Bisphenol A in VUV/UV/peroxymonosulfate system. *Journal of Water Process Engineering, 38*, 101636.https://doi.org/10.1016/j.jwpe.2020.101636

Litter, M.I., Slodowicz, M. 2017. An overview on heterogeneous Fenton and photoFenton reactions using zerovalent iron materials. *20*.doi:10.1515/jaots-2016-0164

Liu, X., Li, H., Gao, S., Bai, Z., Tian, J. 2022. Peroxymonosulfate activation by different iron sulfides for bisphenol-A degradation: Performance and mechanism. *Separation and Purification Technology, 289*, 120751.https://doi.org/10.1016/j.seppur.2022.120751

Lv, X., Xu, J., Jiang, G., Xu, X. 2011. Removal of chromium(VI) from wastewater by nanoscale zero-valent iron particles supported on multiwalled carbon nanotubes. *Chemosphere, 85*, 1204-1209.https://doi.org/10.1016/j.chemosphere.2011.09.005

Marty, M.S., Carney, E.W., Rowlands, J.C. 2011. Endocrine Disruption: Historical Perspectives and Its Impact on the Future of Toxicology Testing. *Toxicological Sciences*, *120*, S93-S108.10.1093/toxsci/kfq329

Neta, P., Grodkowski, J., Ross, A.B. 1996. Rate Constants for Reactions of Aliphatic Carbon- Centered Radicals in Aqueous Solution. *Journal of Physical and Chemical Reference Data, 25*, 709-1050.10.1063/1.555978

Pan, F., Chen, T., Cai, M., Wu, F., You, Z., Li, J. 2021. Fabrication of large-surface-area graphitized carbons by potassium hydroxide-promoted catalytic graphitization. *Materials Research Bulletin, 140*, 111333.https://doi.org/10.1016/j.materresbull.2021.111333

Pestovsky, O., Bakac, A. 2006. Aqueous Ferryl(IV) Ion: Kinetics of Oxygen Atom Transfer To Substrates and Oxo Exchange with Solvent Water. *Inorganic Chemistry, 45*, 814-820.10.1021/ic051868z

Phan, H.T.B., Nguyen, A.Q.K., Ahn, Y.-Y., Kim, K., Kim, S., Kim, J. 2022. Visible light-induced degradation of propranolol with peroxymonosulfate as an oxidant and a radical precursor. *Separation and Purification Technology, 289*, 120764.https://doi.org/10.1016/j.seppur.2022.120764

Ren, Y., Ma, J., Lee, Y., Han, Z., Cui, M., Wang, B., Long, M., Khim, J. 2021. Reaction of activated carbon zerovalent iron with pentachlorophenol under anaerobic conditions. *Journal of Cleaner Production, 297*, 126748.https://doi.org/10.1016/j.jclepro.2021.126748

Romanucci, V., Siciliano, A., Guida, M., Libralato, G., Saviano, L., Luongo, G., Previtera, L., Di Fabio, G., Zarrelli, A. 2020. Disinfection by-products and ecotoxic risk associated with hypochlorite treatment of irbesartan. *Science of The Total Environment, 712*, 135625.https://doi.org/10.1016/j.scitotenv.2019.135625

Su, H., Fang, Z., Tsang, P.E., Zheng, L., Cheng, W., Fang, J., Zhao, D. 2016. Remediation of hexavalent chromium contaminated soil by biochar-supported zero-valent iron nanoparticles. *Journal of Hazardous Materials, 318*, 533-540.https://doi.org/10.1016/j.jhazmat.2016.07.039

Sun, H., Zhou, G., Liu, S., Ang, H.M., Tadé, M.O., Wang, S. 2012. Nano-Fe^0 encapsulated in microcarbon spheres: synthesis, characterization, and environmental applications. *ACS Appl Mater Interfaces, 4*, 6235-6241.10.1021/am301829u

Takdastan, A., Kakavandi, B., Azizi, M., Golshan, M. 2018. Efficient activation of peroxymonosulfate by using ferroferric oxide supported on carbon/UV/US system: A new approach into catalytic degradation of bisphenol A. *Chemical Engineering Journal, 331*, 729-743.https://doi.org/10.1016/j.cej.2017.09.021

Tan, W., Ruan, Y., Diao, Z., Song, G., Su, M., Hou, L.a., Chen, D., Kong, L., Deng, H. 2021. Removal of levofloxacin through adsorption and peroxymonosulfate activation using carbothermal reduction synthesized nZVI/carbon fiber. *Chemosphere, 280*, 130626.https://doi.org/10.1016/j.chemosphere.2021.130626

Thomas, N., Dionysiou, D.D., Pillai, S.C. 2021. Heterogeneous Fenton catalysts: A review of recent advances. *Journal of Hazardous Materials, 404*, 124082.https://doi.org/10.1016/j.jhazmat.2020.124082

Wang, B., Zhu, C., Ai, D., Fan, Z. 2021. Activation of persulfate by green nano-zero-valent iron-loaded biochar for the removal of p-nitrophenol: Performance, mechanism and variables effects. *Journal of Hazardous Materials, 417*, 126106.https://doi.org/10.1016/j.jhazmat.2021.126106

Wang, L., Zhao, Y., Li, Y., Yao, B., Zhang, C., Zhang, W., Niu, L., Zhang, H. 2022. Fe-loaded biochar facilitates simultaneous bisphenol A biodegradation and efficient nitrate reduction: Physicochemical properties and biological mechanism. *Journal of Cleaner Production, 372*, 133814.https://doi.org/10.1016/j.jclepro.2022.133814

Wang, M., Cheng, W., Wan, T., Hu, B., Zhu, Y., Song, X., Sun, Y. 2019a. Mechanistic investigation of U(VI) sequestration by zero-valent iron/activated carbon composites. *Chemical Engineering Journal, 362*, 99-106.https://doi.org/10.1016/j.cej.2018.12.138

Wang, R., Ma, X., Liu, T., Li, Y., Song, L., Tjong, S.C., Cao, L., Wang, W., Yu, Q., Wang, Z. 2020. Degradation aspects of endocrine disrupting chemicals: A review on photocatalytic processes and photocatalysts. *Applied Catalysis A: General, 597*, 117547.https://doi.org/10.1016/j.apcata.2020.117547

Wang, S., Zhao, M., Zhou, M., Li, Y.C., Wang, J., Gao, B., Sato, S., Feng, K., Yin, W., Igalavithana, A.D., Oleszczuk, P., Wang, X., Ok, Y.S. 2019b. Biochar-supported nZVI (nZVI/BC) for contaminant removal from soil and water: A critical review. *Journal of Hazardous Materials, 373*, 820-834.https://doi.org/10.1016/j.jhazmat.2019.03.080

Wei, Z., Villamena, F.A., Weavers, L.K. 2017. Kinetics and Mechanism of Ultrasonic Activation of Persulfate: An in Situ EPR Spin Trapping Study. *Environmental Science & Technology, 51*, 3410-3417.10.1021/acs.est.6b05392

Wijekoon, K.C., Hai, F.I., Kang, J., Price, W.E., Cath, T.Y., Nghiem, L.D. 2014. Rejection and fate of trace organic compounds (TrOCs) during membrane distillation. *Journal of Membrane Science, 453*, 636-642.https://doi.org/10.1016/j.memsci.2013.12.002

Wu, Y., Monfort, O., Dong, W., Brigante, M., Mailhot, G. 2019. Enhancement of iron-mediated activation of persulfate using catechin: From generation of reactive species to atenolol degradation in water. *Science of The Total Environment, 697*, 134188.https://doi.org/10.1016/j.scitotenv.2019.134188

Xu, J., Wang, X., Pan, F., Qin, Y., Xia, J., Li, J., Wu, F. 2018. Synthesis of the mesoporous carbon-nano-zero-valent iron composite and activation of sulfite for removal of organic pollutants. *Chemical Engineering Journal, 353*, 542-549.https://doi.org/10.1016/j.cej.2018.07.030

Yan, J., Han, L., Gao, W., Xue, S., Chen, M. 2015. Biochar supported nanoscale zerovalent iron composite used as persulfate activator for removing trichloroethylene. *Bioresource Technology, 175*, 269-274.https://doi.org/10.1016/j.biortech.2014.10.103

Yan, S., Shi, Y., Tao, Y., Zhang, H. 2019a. Enhanced persulfate-mediated photocatalytic oxidation of bisphenol A using bioelectricity and a g-C3N4/Fe2O3 heterojunction. *Chemical Engineering Journal, 359*, 933-943.https://doi.org/10.1016/j.cej.2018.11.093

Yan, Z.-r., Zhu, Y.-y., Meng, H.-s., Wang, S.-y., Gan, L.-h., Li, X.-y., Xu, J., Zhang, W. 2019b. Insights into thermodynamic mechanisms driving bisphenol A (BPA) binding to extracellular polymeric substances (EPS) of activated sludge. *Science of The Total Environment, 677*, 502-510.https://doi.org/10.1016/j.scitotenv.2019.04.413

Zarrelli, A., DellaGreca, M., Parolisi, A., Iesce, M.R., Cermola, F., Temussi, F., Isidori, M., Lavorgna, M., Passananti, M., Previtera, L. 2012. Chemical fate and genotoxic risk associated with hypochlorite treatment of nicotine. *Science of The Total Environment, 426*, 132-138.https://doi.org/10.1016/j.scitotenv.2012.03.047

Zhang, L., Shen, S. 2020. Adsorption and catalytic degradation of sulfamethazine by mesoporous carbon loaded nano zero valent iron. *Journal of Industrial and Engineering Chemistry, 83*, 123-135.https://doi.org/10.1016/j.jiec.2019.11.020

Zhao, C., Shao, B., Yan, M., Liu, Z., Liang, Q., He, Q., Wu, T., Liu, Y., Pan, Y., Huang, J., Wang, J., Liang, J., Tang, L. 2021. Activation of peroxymonosulfate by biochar-based catalysts and applications in the degradation of organic contaminants: A review. *Chemical Engineering Journal, 416*, 128829.https://doi.org/10.1016/j.cej.2021.128829

Zhou, D., Chen, L., Zhang, C., Yu, Y., Zhang, L., Wu, F. 2014. A novel photochemical system of ferrous sulfite complex: Kinetics and mechanisms of rapid decolorization of Acid Orange 7 in aqueous solutions. *Water Research, 57*, 87-95.https://doi.org/10.1016/j.watres.2014.03.016

Zhu, H., Jia, Y., Wu, X., Wang, H. 2009. Removal of arsenic from water by supported nano zero-valent iron on activated carbon. *Journal of Hazardous Materials, 172*, 1591-1596.https://doi.org/10.1016/j.jhazmat.2009.08.031

Zhuang, P., Lin, W., Tian, B., Shih, T.-m., Cai, W. 2017. Ultraviolet-light-induced electron transfer between chlorine anions and graphene. *Carbon, 123*, 380-384.https://doi.org/10.1016/j.carbon.2017.07.084